

The ALPINE-ALMA [CII] survey

Survey strategy, observations and sample properties of 118 star-forming galaxies at $4 < z < 6$

O. Le Fèvre¹, M. Béthermin¹, A. Faisst², P. Capak^{2,27,28}, P. Cassata^{4,5}, J.D. Silverman^{6,32}, D. Schaerer^{7,8}, L. Yan²³, G.C. Jones^{15,16}, R. Amorin^{12,13}, S. Bardelli¹¹, M. Boquien¹⁴, A. Cimatti^{9,10}, M. Dessauges-Zavadsky⁷, M. Giavalisco¹⁷, N.P. Hathi¹⁷, Y. Fudamoto^{7,25}, S. Fujimoto^{25,26}, M. Ginolfi⁷, C. Gruppioni¹¹, S. Hemmati²⁸, E. Ibar²⁰, A. Koekemoer¹⁷, Y. Khusanova¹, G. Lagache¹, B.C. Lemaux³, F. Loiacono^{9,11}, R. Maiolino^{15,16}, C. Mancini^{4,5}, D. Narayanan^{27,30,31}, L. Morselli⁴, Hugo Méndez-Hernández²⁰, P.A. Oesch⁷, F. Pozzi⁹, M. Romano⁴, D. Riechers^{29,22}, N. Scoville³³, M. Talia^{9,11}, L. A. M. Tasca¹, R. Thomas¹⁸, S. Toft^{27,28}, L. Vallini²¹, D. Vergani¹¹, F. Walter²³, G. Zamorani¹¹, and E. Zucca¹¹

(Affiliations can be found after the references)

Received ; accepted

ABSTRACT

The ALMA-ALPINE [CII] survey (A2C2S) aims at characterizing the properties of a sample of normal star-forming galaxies (SFGs). ALPINE, the ALMA Large Program to INvestigate 118 galaxies observed in the [CII]-158 μ m line and far Infrared (FIR) continuum emission in the period of rapid mass assembly, right after HI reionization ended, at redshifts $4 < z < 6$. We present the survey science goals, the observational strategy and the sample selection of the 118 galaxies observed with ALMA, with a typical beam size of about 0.7'', or < 6 kpc at the median redshift of the survey. The properties of the sample are described, including spectroscopic redshifts derived from UV-rest frame, stellar masses and star-formation rates obtained from spectral energy distribution (SED) fitting. The observed properties derived from the ALMA data are presented and discussed in terms of the overall detection rate in [CII] and FIR continuum, with the observed signal-to-noise distribution. The sample is representative of the SFG population on the main sequence at these redshifts. The overall detection rate in [CII] is 64%. From a visual inspection of the [CII] data cubes together with the large wealth of ancillary data we find a surprisingly wide range of galaxy types, including 40% mergers, 20% extended and dispersion dominated, 13% compact and 11% rotating discs, the remaining 16% being too faint to be classified. This diversity indicates that a wide array of physical processes must be at work at this epoch, first and foremost galaxy merging. This paper sets a reference sample for the gas distribution in normal SFGs at $4 < z < 6$, a key epoch in galaxy assembly, ideally suited for studies with future facilities like the James Webb Space Telescope and extremely large telescopes.

Key words. Galaxies: high redshift – Galaxies: evolution – Galaxies: formation – Galaxies: star formation

1. Introduction

The mass assembly in galaxies at different epochs proceeds from several physical processes which, together, produce the remarkable observed evolution of the star formation rate density (SFRD) with cosmic time (Silk & Mamon 2012; Madau & Dickinson 2014; Dayal & Ferrara 2018, and references therein). The SFRD first rises during the reionization epoch, to reach a peak at $z \sim 2 - 3$ after a ~ 1 dex increase in ~ 3 Gyr, then decreases by ~ 0.8 dex in ~ 10 Gyr to the current time (Madau & Dickinson 2014; Bouwens et al. 2015). Along with star formation, the total stellar mass density (SMD) in galaxies is observed to rise steeply from early times to $z \sim 2$, followed by a slower increase at $z < 2$ (Ilbert et al. 2013).

At the root of the SFRD and SMD evolution, the transformation of gas into stars in a hierarchical picture of galaxy assembly is a key element. Two main processes are shown from more and more detailed simulations to drive this evolution: gas accretion and galaxy merging (Hopkins et al. 2006; Dekel et al. 2009; Bournaud et al. 2011; Naab & Ostriker 2017). This is expected

to be tempered by feedback processes from gas expelled from galaxies by strong AGN and/or stellar jets and winds (Silk 1997; Hopkins et al. 2008; Silk 2013). While this is appealing from a theoretical and simulation standpoint, there is actually very little observational support towards a comprehensive, consistent, and quantitative picture, particularly at the early cosmic epochs when mass assembly is in a major phase. Galaxy mergers, major and minor, are observed at all epochs (e.g. Conselice 2014), with a major merger rate increasing from the local universe to $z \sim 2$ (e.g. Lotz et al. 2011; López-Sanjuan et al. 2013; Mantha et al. 2018), and possibly flattening to $z \sim 4 - 5$ (e.g. Tasca et al. 2014; Ventou et al. 2017), while gas accretion suffers from weak signatures difficult to identify observationally, and its effects are only identified indirectly (e.g. Bouché et al. 2013). On the other hand, feedback processes are directly measured (e.g. Le Fèvre et al. 2019), thought to affect both the bright and faint end of the galaxy luminosity function ((LF), e.g., Croton et al. 2006; Hopkins et al. 2008; Gabor et al. 2010, 2011), due primarily to AGN and stellar processes, respectively.

To disentangle the relative contributions of these processes, the far infrared (FIR) domain redshifted in the sub-mm for high- z galaxies is proving particularly rich with information. From the

* Based on data obtained with the ALMA observatory, under Large Program 2017.1.00428.L

sub-mm it is now possible to investigate the properties of star-forming galaxies up to the epoch of HI reionization. The [CII]-158 μ m line is the dominant coolant making it one of the strongest FIR lines. The [CII] emission is primarily coming from photodissociation regions (PDR) and cold neutral medium (CNM) of molecular clouds. [CII] at high- z has raised considerable interest as it probes the gas from which stars form in normal galaxies (e.g. Ferrara et al. 2019, and references therein), and then broadly traces star formation activity, offering an important window on galaxy formation (Carilli & Walter 2013; De Looze et al. 2014). This led to the detection of strong [CII] emitters, up to very high redshifts (Capak et al. 2015; Carniani et al. 2017), an easier measurement than the FIR continuum. Searching for [CII] emission, interpreting and simulating the observations, and comparing them with other emission lines such as Lyman- α , has therefore become a major new way of studying high- z galaxies. The strong UV radiation in high- z galaxies results in a non-negligible fraction of [CII] emission from the extended warm ISM (e.g. Capak et al. 2015; Faisst et al. 2017). The [CII] emission together with its morphology provides important information on the SFR and ISM properties (e.g. Vallini et al. 2015; Wellons et al. 2016; Olsen et al. 2017). The FIR continuum emission adjacent to [CII] is near the peak of the FIR emission. It constrains the total FIR luminosity, and provides a measurement of the total SFR when combined with UV continuum measurements. It can also be combined with UV colors and luminosity to construct the Infrared-Excess (L_{FIR}/L_{UV}) vs. UV color diagnostic, providing insight into the spatial distribution of dust, dust grain properties, and metallicity (Reddy et al. 2012; Faisst et al. 2017).

Simulations of forming galaxies during and right after reionization are informing on the possible properties of these galaxies despite the difficulty to take into account early galaxy formation processes during and right after the Epoch of reionization in a consistent way (e.g. Dayal et al. 2013; Maiolino et al. 2015). Specific predictions related to [CII] emission are useful to guide and compare to observations (e.g. Yue et al. 2015; Vallini et al. 2015; Olsen et al. 2017; Kohandel et al. 2019).

This whole domain opened up at high redshift ($z>4$) with the ALMA interferometer becoming fully operational, when it was realized from pilot observations that detecting [CII] for normal galaxies was ubiquitous even with short on-source exposure times (Capak et al. 2015). Galaxies with star formation rates as low as a few $M_{\odot}.yr^{-1}$ have been detected in [CII] at $z\sim 5$ (Riechers et al. 2014; Capak et al. 2015), and [CII] is now detected for galaxies well into the reionization epoch (e.g. Bradač et al. 2017; Harikane et al. 2018; Fujimoto et al. 2019; Sobral et al. 2019).

However, existing observations of [CII] in normal galaxies at these epochs are still scarce. As strong sub-mm sources have primarily been targeted (e.g. Maiolino et al. 2009; Carilli & Walter 2013; Wagg et al. 2012; Riechers et al. 2014), they provide us with a view biased towards the highly star-forming population with $SFR > 1000 M_{\odot}.yr^{-1}$. Normal galaxies, that is galaxies with SFR in the range from ~ 10 to a few hundred solar masses per year, lying on the so-called main sequence at these redshifts (e.g. Speagle et al. 2014; Tasca et al. 2015; Tomczak et al. 2016; Pearson et al. 2018; Khusanova et al. 2019), have not been observed in statistically representative numbers. The Capak et al. (2015) observations proved that this was feasible and prompted us to submit the ALPINE Large Program, largely designed based on the properties of the Capak et al. (2015) sample. A key element was the availability of large samples of these normal galaxies, with accurate *spectroscopic redshifts* (Le Fèvre et al. 2015;

Hasinger et al. 2018) to be able to define ALMA observations with a high success rate in detecting [CII].

This paper presents a general overview of the survey, in combination with papers presenting a detailed account of the data processing, [CII] flux and continuum measurements (Béthermin et al., 2019, in prep.), and ancillary data with physical parameters computation (Faisst et al., 2019, in prep.). The layout of this paper is as follows. In Sect. 2 we present the general ALPINE survey design, with science goals and sample selection as in the original proposal. We give an overview of the ALMA observations as well as a summary of the large amount of ancillary observations available in Sect.3. In Sect.4, we describe the main properties of the sample, including the redshift distribution, detection rates in [CII] and continuum, and observed flux limits. Flux maps of all sample galaxies in the [CII] line are presented in Sect.5. We use these maps, kinematic data, and all ancillary imaging data to perform an empirical visually-based morpho-kinematic classification as described in Sect.6. We summarize in Sect.7.

Throughout the paper we use a Λ CDM cosmology with $H_0 = 70$ km/s/Mpc, $\Omega_{\Lambda} = 0.70$, $\Omega_m = 0.30$. All magnitudes are given in the AB system.

2. ALPINE survey design

2.1. Science goals

The main goals of ALPINE at $4<z<6$ are broadly defined as follows:

- *Characterize the use of [CII] as a SFR indicator at these epochs.* The prevalence of [CII] in high- z galaxies is a promising tool to estimate SFRs of FIR continuum-faint galaxies. While local studies find a good correlation between [CII] and SFR, this relation may change at the lower metallicities of high- z galaxies. There is also evidence that [CII] is often emitted from the diffuse CNM or HII regions in addition to PDRs (Herrera-Camus et al. 2017; Pineda et al. 2013; Vallini et al. 2015), it also traces the diffuse ionized gas, but see (Pavesi et al. 2016, 2019). ALPINE allows calibrating this relation by comparing [CII] derived SFR to other indicators (FIR, UV, SED) over a large range of physical properties.
- *A comprehensive and precise (accuracy better than 20%) measurement of the SFRD at these epochs from UV+FIR continuum and [CII] emission, allowing to constrain the mechanisms which fuel the initial growth of typical galaxies in the early universe.* The total SFRD at $z>4$, a key epoch in galaxy assembly, is a crucial element in understanding galaxy formation. However, it remains a difficult observational measurement, as we do not yet know how much of the star formation is hidden from the wealth of existing deep UV observations. Only a survey selecting sources based on the FIR emission could solve the question but this is currently not feasible for a statistically representative sample, given the small field of view of the ALMA telescope. With ALPINE we follow a stepped approach. Starting from well-studied sources in the UV, the goal is to obtain FIR continuum and [CII] measurements to measure the fraction of their star formation that is hidden by dust. Combined with SFR derived from the UV continuum, this will deliver the total star formation of UV-selected samples.
- *Estimate the remaining fraction of the star formation that may not be traced by UV sign-posts.* In addition to the above, we

aim to use the serendipitous survey assembled by ALPINE on a total area of about 25 square arcminutes to estimate what fraction of star formation is missed in obscured sources. Together, these measurements will result in a first estimate of the [CII] luminosity function and the total SFRD at $4 < z < 6$ consolidated from the UV and FIR.

- *A first detailed characterization of the ISM properties using $L_{\text{FIR}}/L_{\text{UV}}$ and [CII]/FIR diagnostics.* The evolution of [CII] emission and its resolved velocity profile provide important information on the SFR and ISM properties, setting constraints on galaxies dynamical and gas masses. The morphology of the [CII] emission, and more generally of the gas distribution, indicates if star formation is compact or extended, an important element to understand high- z star formation (e.g. Wellons et al. 2016). Beyond the line flux, the FIR continuum emission constrains the total FIR luminosity, and provides a good measurement of the total SFR when combined with UV continuum measurements. The continuum flux can also be combined with UV color and luminosity to construct the IRX- β diagnostic, providing insight into the spatial distribution of dust, dust grain properties, and metallicity (Reddy et al. 2012; Faisst et al. 2017). The [CII] line has also been used as a tracer of the molecular gas content (Hughes et al. 2017; Zanella et al. 2018), shown to be more reliable in low metallicity environments than e.g. CO.
- *Star-forming main-sequence and merger rates at $z > 4$.* The SFRD across cosmic time as well as the shape and scatter of the star forming main sequence (MS) in the SFR-stellar mass plane provide important constraints on the starburst duty cycle and merger rate of galaxies (Rodighiero et al. 2011; Guo et al. 2013; Tomczak et al. 2016; Tacchella et al. 2015) and ultimately their mass growth (cold accretion vs. merger paradigm Dekel et al. 2009; Davé et al. 2011; Tasca et al. 2014; Faisst et al. 2017). The independent SFR measurements from FIR and [CII] in addition to SED fitting will help constrain the true scatter of the MS at $z > 4$ as a function of stellar mass. The comparison to $H\alpha$ based SFRs on < 100 Myr timescales from Spitzer colors (Faisst et al. 2017) or later from JWST spectroscopy will allow us to put constraints on the starburst duty cycles. Following the serendipitous [CII] detections of UV-faint galaxies in interaction with the main targets (extrapolating from Capak et al. 2015, we expect to find ~ 15 -30 mergers in ALPINE) which will allow us to model the merger rates and thus constrain the dominant mode of mass build-up of galaxies in the early universe.
- *A first measurement of dynamical masses from spectrally resolved [CII],* combined with stellar masses and statistical estimates of dark matter halo masses to measure dust content, gas fraction, and their evolution. The [CII] line is an excellent tracer of gas dynamics, which can be used in the same way as $H\alpha$ at $z < 2$ (e.g. Förster Schreiber et al. 2009; Epinat et al. 2012; Molina et al. 2017). The ALPINE observations aim to provide a first approach at dynamical measurements at $4 < z < 6$, deep into the epoch of early galaxy formation. Dynamical masses (M_{dyn}) can be estimated from the velocity dispersion σ_{vel} derived from the [CII] line emission, while the brightest galaxies resolved in [CII] enable a direct measurement of the [CII] extent. It is expected that resolved galaxy sizes (Ribeiro et al. 2016) will lead to a useful dynamical mass measurement for $\sim 20\%$ of the sample. Upper limits will be derived for the rest of the sample.
- *Gas fractions at $z > 4$:* Comparing M_{dyn} to reliable emission line corrected stellar masses from deep Spitzer imaging (Laigle et al. 2016, and Faisst et al. (2019, in prep.)), and

dust mass estimates from FIR measurements (Scoville et al. 2016) will put the first direct constraints on the gas fractions f_{gas} at $z > 4$. The contribution of dark matter to the total velocity component at $1-2R_e$ is expected to be low (Barnabè et al. 2012), but can be estimated by matching our sample to the output of state-of-the-art hydro-dynamical simulations such as EAGLE (McAlpine et al. 2016) FIRE (Hopkins et al. 2014), or Illustris TNG (Davé et al. 2019), or estimating average dark halo masses from HOD modeling of the correlation function (Durkalec et al. 2015). Combined with SFRs derived from UV, FIR, [CII], and $H\alpha$, this will constrain SFR efficiencies and gas depletion times, thus providing insight into the emergence and growth of massive galaxies (Tacconi et al. 2013; Genzel et al. 2015; Dessauges-Zavadsky et al. 2017; Tacconi et al. 2018).

- *The role of feedback processes in the early Universe.* The prevalence of feedback processes from galactic winds produced by massive stars, supernovae and AGN will be studied using kinematic diagnostics and [CII] line profiles (see from ALPINE, Ginolfi et al. 2019).

2.2. Sample selection

The sample is drawn from large spectroscopic survey samples of normal SFGs in the COSMOS (Scoville et al. 2007b) and ECDFS fields (Giacconi et al. 2002).

A key element is that galaxies must have a reliable spectroscopic redshift in $4.4 < z_{\text{spec}} < 5.9$ ($< z_{\text{spec}} > \sim 4.7$), excluding $4.65 < z < 5.05$ where [CII] falls in a low transmission atmospheric window. Galaxies are UV-selected (see Le Fèvre et al. 2015, for more details) with $L_{\text{UV}} > 0.6L^*$ to include most of the star formation traced by the UV, and excluding type I AGN identified from broad spectral lines. Accurate redshifts come from extensive spectroscopic campaigns at the VLT (VUDS, Le Fèvre et al. 2015) and Keck (DEIMOS, Hasinger et al. 2018). While the VUDS sample is unbiased against Lyman- α emitters or absorbers (Khusanova et al. 2019), Lyman- α emitters may be over-represented in the DEIMOS sample; this will need to be taken into account in subsequent analysis of the whole ALPINE sample. Galaxies in the parent sample were mostly selected based on their photometric redshifts based on SED fitting, followed by UV spectroscopy to secure the redshift, (see Le Fèvre et al. 2015; Hasinger et al. 2018) for more details. The absolute UV luminosity cut ($M_{\text{UV}} < -20.2$) is equivalent to $\text{SFR} > 10 M_{\text{sun}} \cdot \text{yr}^{-1}$, as seen in Fig. 1. Using the De Looze et al. (2014) relation for high- z galaxies (supported by Capak et al. 2015), this SFR limit is equivalent to $L_{[\text{CII}]} > 1.2 \times 10^8 L_{\odot}$. Some galaxies with SFR below ~ 1 solar masses per year were included when made possible by the observational setup. This sample is representative of the overall SFG population, rather than ULIRGS (Ultra Luminous Infra Red Galaxies), that is mostly of galaxies positioned on or near the so-called main sequence in the SFR versus M_{star} plane observed at these redshifts (e.g. Speagle et al. 2014; Tasca et al. 2015; Tomczak et al. 2016; Pearson et al. 2018; Khusanova et al. 2019), with M_{star} and SFR derived from SED fitting setting the redshift to the spectroscopic redshift. We selected 118 galaxies based on these criteria. More details on the sample properties are given in Sect. 4.

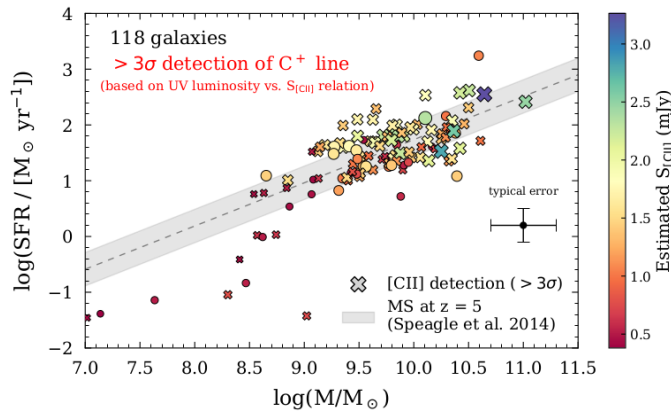


Fig. 1. Stellar mass vs. SFR distribution of ALPINE sources as selected prior to ALMA observations, colored by expected [CII] line peak flux estimated from Capak et al. (2015). M_{star} and SFR were obtained from SED fitting of the multi-wavelength photometry available at the start of this program (see Faisst et al., in prep. for more details). The cross represents the average 1σ uncertainty. The large proposed sample aims to quantify average trends over a large range of galaxy properties. Those galaxies detected at $>3\sigma$ in [CII] are identified with crosses. ALPINE provides [CII] emission line measurements at $>3.5\sigma$ for 63% of these galaxies (see text).

3. Observational data

3.1. ALMA

Here we summarize the observations, pointing to Béthermin et al. (2019, in prep.) for an extensive description of observations and data processing, following the best practice with customized pipelines based on the Common Astronomy Software Applications (CASA) tools (McMullin et al. 2007).

This program was awarded an ALMA Large Program status under number 2017.1.00428.L for a total of 69 hours including on-source time, calibrations, and overheads. ALMA observations were carried out in Band-7 starting in May 2018 during Cycle 5 and completed in February 2019 in Cycle 6. Each target was observed for about 30 minutes and up to one hour of integration time, with the phase centers centered on the UV rest-frame positions of the sources. The availability of spectroscopic redshifts allowed to accurately set the main spectral window on the expected [CII] frequencies. In order to minimize overheads, targets making use of a similar setup were grouped. The other side spectral windows were then used for FIR continuum measurements, an important component of this program as continuum measurements can be used as a proxy for the total FIR, therefore for the SFR. The main calibration for the [CII]-SFR relation will partly rely on those galaxies with continuum data.

At these redshifts, the velocity width of one ALMA bandpass in band-7 is as narrow as ~ 3000 km/s per sideband. Samples with photometric redshifts accurate to $\sim 0.05 \times (1+z)$ at these redshifts (e.g. Ilbert et al. 2013), would have added a considerable uncertainty on the detection of [CII] and associated incompleteness, making it more hazardous to build e.g. the [CII] luminosity function. With an accuracy of a few hundred km/s even at low spectral resolution from optical (UV rest-frame) spectroscopy (Le Fèvre et al. 2015), the availability of z_{spec} is therefore a key element of this program ensuring a high [CII] detection rate and, for those galaxies which would be undetected, setting stringent upper limits.

We use the TDM mode of the ALMA correlator, which offers the largest bandwidth to optimize the continuum sensitivity. The

resolution varies with redshift from 26 to 35 km/s. We assumed 235 km/s FWHM line width (or $\sigma \sim 100$ km/s), which is the average width measured in the Capak et al. (2015) sample. Emission lines were thus expected to be spectrally resolved giving the possibility to measure the line width when the SNR is sufficient.

We prioritize detection over spatial resolution, and with the typical size of the Capak et al. (2015) sources being 0.5-0.7 arcsec, we elected to use ALMA array configurations offering an angular resolution not larger than 0.7 arcsec. The median beam size of the ALMA observations is then about 0.7 arcsec FWHM.

We provide the ALPINE source list in Table 1 including (RA, DEC) positions, spectroscopic redshift, [CII] SNR, when detected above 3.5σ , and flux limits when the source is undetected $< 3.5\sigma$. 3.5σ is the threshold at which our simulation indicates a 95% reliability; see Béthermin et al. 2019 (in prep.). The SNR is computed as the ratio between peak fluxes and rms in the [C II] velocity-integrated maps, as listed in Table 2.

3.2. Ancillary data

The choice of the COSMOS and ECDFS fields to select the sample is driven by the availability of z_{spec} as described above and also by the large suite of multi-wavelength data available in these fields, as is extensively described in Faisst et al. (2019, in prep.). These data enable to construct the SED for each galaxy, essential to measure the fundamental physical parameters needed to assess the general properties of the observed galaxy population.

All ALPINE targets in the COSMOS field (Scoville et al. 2007a) are covered by HST F814W i-band imaging (Koekemoer et al. 2007), Subaru optical imaging (Taniguchi et al. 2007), deep NIR YJHK imaging from the UltraVista Survey (McCracken et al. 2012), SPITZER 3.6 and $4.5 \mu\text{m}$ imaging (Sanders et al. 2007), with good X-ray coverage with both XMM-Newton (Hasinger et al. 2007) and Chandra (Elvis et al. 2009; Civano et al. 2016) as well as radio waves (Smolčić et al. 2017). While most of the imaging is done under point-spread functions (PSF) with similar spatial resolution as the ALMA imaging, typically FWHM ~ 0.8 arcsec, the HST F814W i-band imaging provides a sharper look with a PSF ~ 0.1 arcsec. A source catalog with matched photometry is available as described in Laigle et al. (2016).

The data that we use in the area of the ECDFS is from the CANDELS survey (Grogin et al. 2011; Koekemoer et al. 2011).

The derivation of key physical quantities from the SED fitting, including stellar mass, SFR, dust extinction, is described in detail in Faisst et al. (2019, in prep.)

4. Sample properties

4.1. Redshift distribution

The redshift distribution of the ALPINE sample is presented in Fig. 2 for all galaxies as well as those with [CII] detected at more than 3.5σ above the noise. There are two separate peaks in the $N(z)$ owing to the atmospheric visibility windows.

Comparing the redshifts obtained from the UV spectra to those obtained from [CII], which defines the systemic redshift of the gas component, allows one to probe the velocity difference between the stellar and gas components. This will be explored in a forthcoming paper.

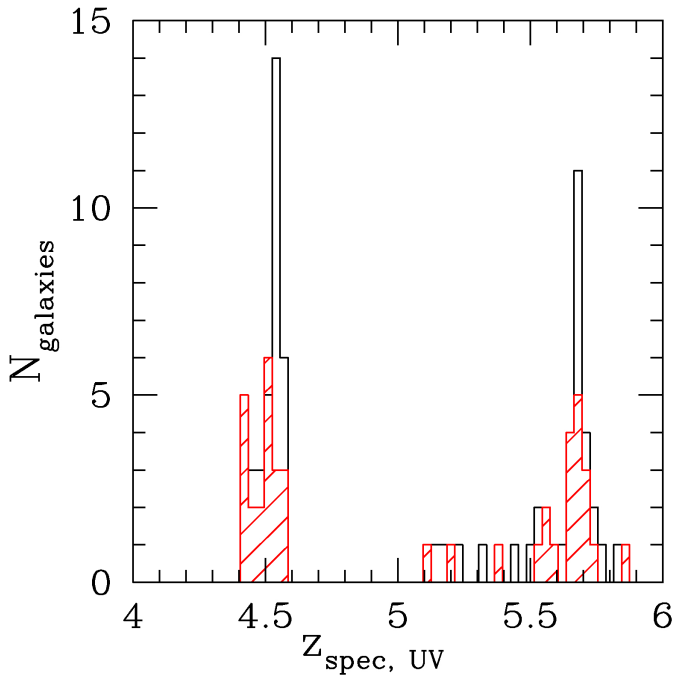


Fig. 2. Redshift distribution of the ALPINE sample, using the spectroscopic redshifts measured from the UV rest-frame spectra (Le Fèvre et al. 2015; Hasinger et al. 2018). The empty histogram is for all observed sources while the red shaded histogram is for those sources with [CII] measured at more than 3.5σ above the noise.

4.2. Detection rate in [CII] and continuum

The Signal to noise ratio (SNR) of the integrated [CII] line flux detections are presented in Fig. 3. The median SNR is ≈ 6.2 for the detected objects. See Béthermin et al. (2019, in prep.) for more details. Taking 3.5σ as a conservative detection limit (purity $> 95\%$) owing to the somewhat correlated noise of ALMA interferometric imaging, ALPINE detected [CII] in 75 galaxies out of 118, hence a success rate of $\approx 64\%$ as presented in Tab. 1 and 2. In the continuum adjacent to [CII], 25 galaxies, or 21%, are detected. These rates are quite impressive given the redshift of the sources and short integration times. The lower continuum detection rate is as expected from the SED models in the FIR (Béthermin et al. 2017). Stacking of the continuum data will allow to place useful constraints on the fainter emitters. The SNR of most other targets varies in the range from 0.5 to 3, providing useful upper limits.

We identify a number of line emitters detected serendipitously in the data cubes. These will be matched with the ancillary source catalogues in these fields, attempting to identify whether the line is [CII] at the redshift of the targeted sample, or some other line at lower redshift (Loiacono et al., in prep.).

4.3. Positional offsets between [CII] and UV rest-frame

Positional offsets between the [CII] flux distribution and the UV rest-frame images have been reported for galaxies at similar redshifts as the ALPINE sample (e.g. Carniani et al. 2017). Offsets from frame centers representing the UV position are clearly evident for some objects on Figs. 4 to 10. A preliminary analysis shows that for most (90%) of the sources the differences in RA and DEC are well represented by Gaussians centered at zero offset with a sigma of about $0.18''$, consistent with the typical uncertainty in position of the ALMA sources, and a significant

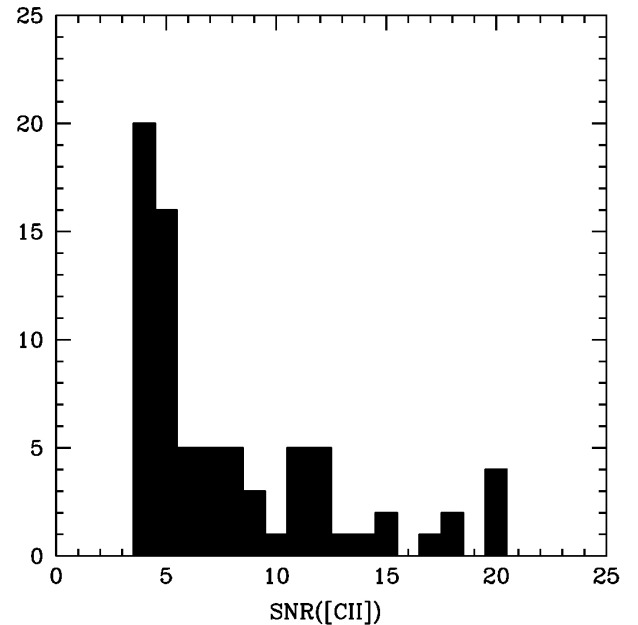


Fig. 3. Signal to noise ratio (SNR) of the integrated [CII] line flux for those sources with [CII] measured at more than 3.5σ above the noise.

offset (up to a maximum of $\sim 1''$) is present only for 10% of the sources. See Faisst et al. (2019, in prep.) for more details.

5. [CII] flux maps

Images in the [CII] line of sources with [CII] detected at more than 3.5σ are presented in Fig. 4, 6, 8, and Fig. 10. These so-called [CII] 'flux images' (flux maps thereafter) are produced using the CLEAN algorithm and the immoments routine, optimally extracted using an iterative process to determine the line profile of the source and then collapse channels $[f_{cen} - FWHM; f_{cen} + FWHM]$, where f_{cen} is the central frequency of [CII], which can be a posteriori confirmed to be different from the UV (see Béthermin et al., 2019, in prep.). These flux maps are compared to HST i-band F814W images (Koekemoer et al. 2007, 2011) in Figs. 5, 7, 9, and 11), representing the UV rest-frame, with [CII] contours overlaid.

These images give a first view of the shape of the [CII] emission in normal galaxies at $4 < z < 6$. There are several facts worth noting. Even though the observations were carried out with a beam size providing moderate spatial resolution with $FWHM \sim 0.7''$, about two thirds of the sources are resolved in [CII]. This means that intrinsic (total) sizes as seen in atomic gas must be about the size of the beam, or a significant fraction thereof, hence physical source sizes reaching several kiloparsecs. By itself this fact gives an indication that physical processes at work in those galaxies are puffing up their sizes beyond being compact. Another striking evidence from these images is the large diversity of [CII] emission morphology. Some objects appear as very extended (e.g. bottom-left object COSMOS 881725 in Fig. 8), some others with double merger-like components (e.g. third row, second from left object COSMOS 351640 in Fig. 4), while others are compact (unresolved). This diversity must also reflect a diversity in the physical processes at work.

We dwell more on this in attempting a visual classification in the following Sect. 6, and future papers will focus on the quantitative properties of the [CII] emission in the different classes of the ALPINE sample.

6. Morpho-Kinematic classification

As presented in Sect. 5, the [CII] emission appears spatially very diverse. As we have at our disposal not only the flux maps, but the full (α, δ , velocity) 3D data-cubes for all sources as well as all ancillary information presented in Sect. 3.2, we are able to perform an empirical visual-based morpho-kinematic classification, as discussed below.

The observational data were assembled in one slide per object, including the ALMA data with flux map, the channel maps cut in 25 km/s velocity intervals, the velocity field map (moment 1), position-velocity (PV) diagrams projected along the major and minor axes of the velocity map, and the integrated 1D [CII] spectrum, together with multi-band optical and NIR images including HST ACS F814W i-band and/or WFC3-F160W images when available, as presented in Fig. 12. All these data served as input to object classification described below.

Following previous work from 3D integral field spectroscopy using H α (e.g. Förster Schreiber et al. 2009; Epinat et al. 2012), we define the following morpho-kinematic classes:

- Class 1: Rotator. This class is defined for galaxies satisfying the following criteria:
 - Smooth transition between intensity channel maps
 - Obvious gradient in velocity field map (Moment 1)
 - Tilted PV along the major axis, straight PV on the minor axis
 - Possible double-horned profile in spectrum
 - Single component in ancillary data
- Class 2: Pair-Merger (major or minor), interacting system:
 - Complex behavior in channel maps
 - Separate components in flux maps and/or PV diagrams
 - Multiple components in ancillary data
- Class 3: Extended Dispersion dominated
 - No positional shift of emission across intensity channel maps
 - Straight PV diagrams
 - Extended beyond the ALMA beam in flux maps
- Class 4: Compact Dispersion dominated
 - No positional shift of emission across intensity channel maps
 - Straight PV diagrams
 - Unresolved in flux maps
- Class 5: too weak to be classified

All the observational material described above was then visually inspected independently by eight people in the team, each one assigning a class to each ALPINE object. This provided a statistical basis to estimate the mode of the classification for each object, and a rough dispersion obtained as the average of the difference between the mode and each individually-measured class. To mitigate somewhat the well-known effect of a dominant class not necessarily being ‘the truth’ (e.g. most people missing some key evidence while only a few spotted it), the mode and extremes of the classification were examined by two people who proposed to the team the class satisfying all identified evidence. One last iteration was then performed, with individual team members asked to identify the objects for which they were in most disagreement with, followed by a last round to agree on

a final classification. This led to the final classification listed in Table 1.

The distribution in the different classes is presented in Fig. 13. We find 40% of galaxies in the merger class 2, 20% in the extended and dispersion dominated class 3, 13.3% rotating discs in class 1, 10.7% compact in class 4, and , the remaining 16% of the sample being too difficult to classify (class 5). We note the high fraction of mergers, indicating that mass assembly through merging is frequent at these redshifts for normal main sequence SFGs. Preliminary examination of spatial and velocity information indicates that most merging systems would merge within 0.5 to 1 Gyr (e.g. the triple merger system presented by Jones et al. 2019), which then means that most of these mergers would end-up forming one single galaxy by $z \sim 2.5$. Merging systems observed at sub-mm wavelengths have been reported previously, but for more starburst-like objects (e.g. recently, Danielson et al. 2017; Tadaki et al. 2018; Zhang et al. 2018; Díaz-Santos et al. 2018; Hodge et al. 2019). The presence of extended [CII] nebulae in Class 3 is also quite striking in indicating that large extended gas reservoirs were readily available to fuel star formation right after reionization ended.

The properties of galaxies in these different samples will be extensively described in future papers from the ALPINE team. It may well be that some objects in Class 4 would appear as rotators when observed under higher spatial resolution, as seen in near-IR integrated field observations of $z \sim 2$ massive galaxies (e.g. ?). On the other hand, galaxies at $z=1-3$ with stellar masses comparable to the ALPINE sample show a larger proportion of dispersion-dominated galaxies than galaxies with higher masses.

7. Summary and conclusions

The ALMA-ALPINE [CII] survey (A2C2S) provides an unprecedented view of a representative sample of 118 star-forming galaxies observed in their assembly right after the end of HI reionization at redshifts $4 < z < 6$. Galaxies are selected on the basis of an existing reliable spectroscopic redshift, and using the SED-based SFR to predict the [CII] flux using the De Looze et al. (2014) relation and selecting SFR such that $L[\text{CII}] > 1.2 \times 10^8 L_\odot$. The overall detection rate is 64% for galaxies detected in [CII] 3.5σ above the noise, 21% in the continuum, down to a flux limit of $0.07 \text{ Jy. km. s}^{-1}$ per beam in the continuum. We present the ALPINE survey strategy and sample properties and we present the projected [CII] flux maps. Combining these maps with velocity channel maps, velocity field, and all available ancillary information, we establish a classification scheme. We find a surprisingly wide range of galaxy types, including 40% mergers, 20% extended and dispersion dominated, 13.3% rotating discs, 10.7% compact, the remaining 16% being too faint to be classified. This diversity of types indicates that several physical processes are at work to assemble mass in these galaxies, first and foremost galaxy merging. While galaxy merging is commonly associated to starbursts above the main sequence, at least up to $z \sim 3$, merging systems in ALPINE at $z \sim 4.7$ lie mainly on the MS, and therefore merging is also a dominant process for normal SFGs at this epoch. This will be further investigated in future papers.

The ALPINE sample offers a unique opportunity to study galaxies as they are assembling. This paper is the first in a series, and future papers will present analyses of specific populations as well as general statistical properties. ALPINE galaxies are ideally suited for follow-up with JWST and the forthcoming ELTs.

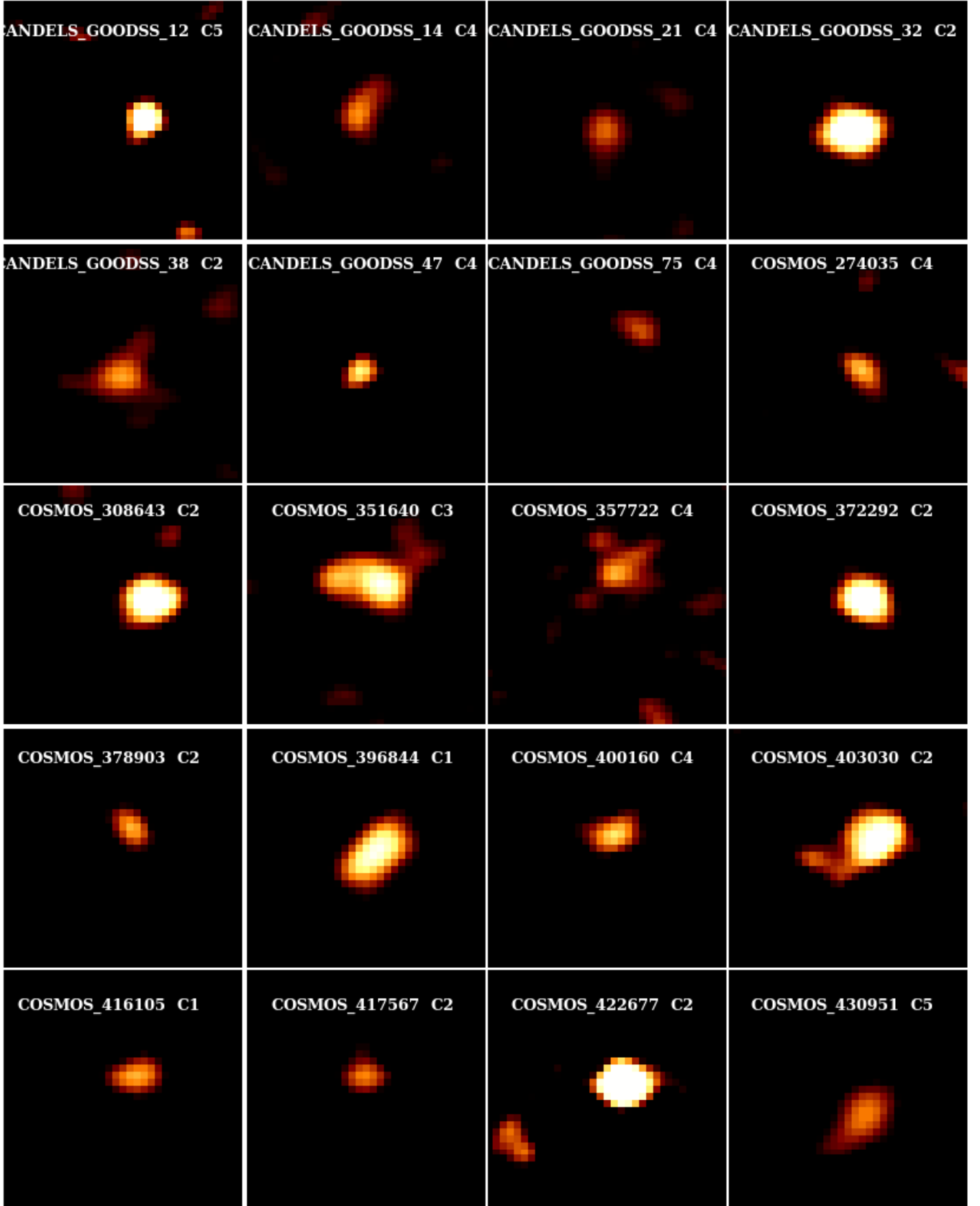


Fig. 4. Velocity-integrated [C II] flux maps obtained collapsing the cube channels containing the [C II] line (see text). Each panel is $5'' \times 5''$ or about 33×33 kpc at the mean redshift $z = 4.7$ of the survey, centered on the position of the source in the UV rest-frame based on HST-814W images. The object name and morpho-kinematic Class (see Sect. 6) are indicated on top of each sub-panel.

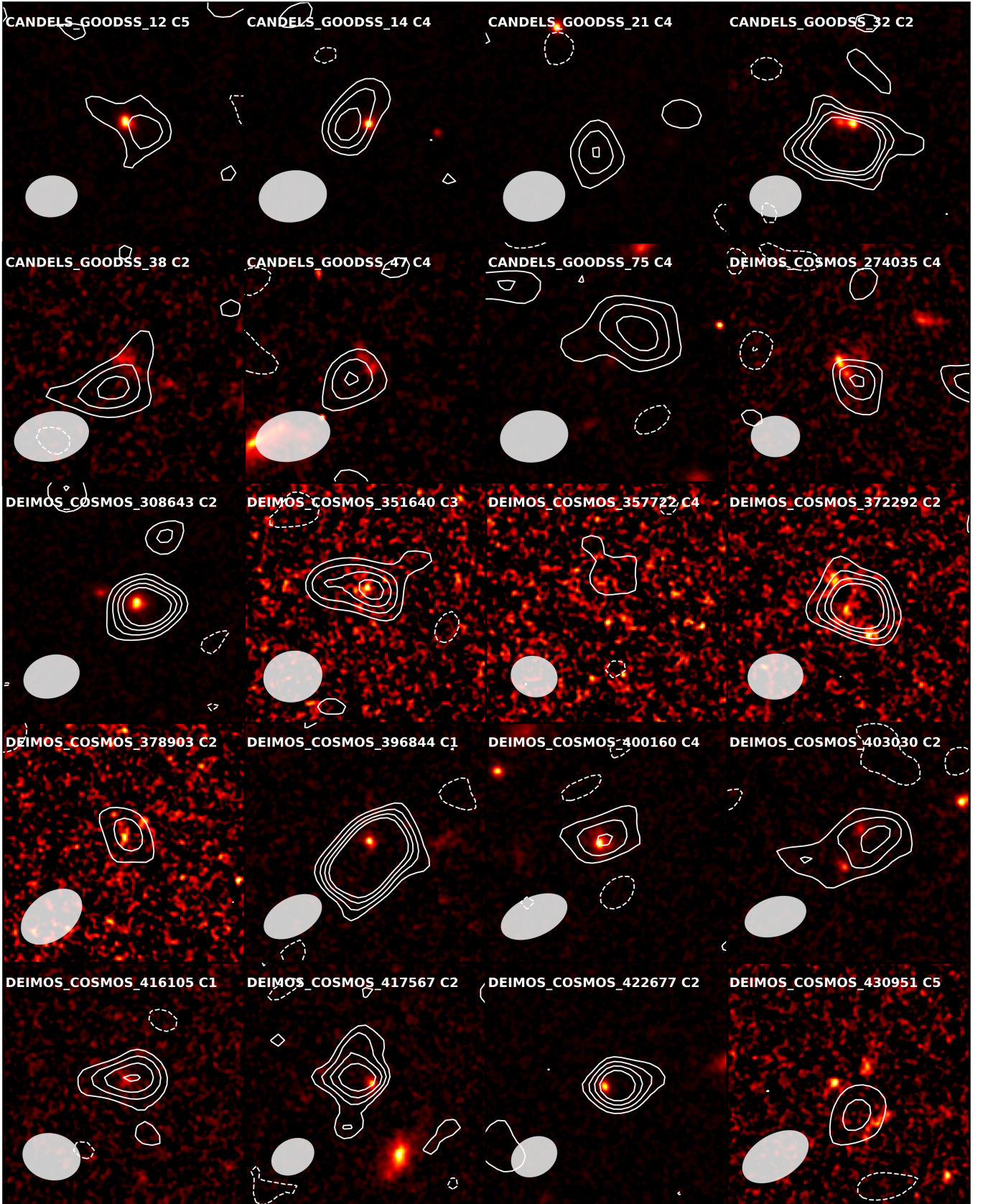


Fig. 5. HST F814W images (Koekemoer et al. 2007, 2011) corresponding to [CII] flux maps in Fig. 4. Each panel is $5'' \times 5''$ or about 33×33 kpc at the mean redshift $z = 4.7$ of the survey, centered on the position of the source in the UV rest-frame HST-814W images. The white contours represent the distribution of the [CII] flux from Fig. 4, and the grey-filled ellipse is the ALMA beam size.

Acknowledgements. This paper is based on data obtained with the ALMA Observatory, under Large Program 2017.1.00428.L. ALMA is a partnership of ESO (representing its member states), NSF(USA) and NINS (Japan), together with NRC (Canada), MOST and ASIAA (Taiwan), and KASI (Republic of Korea), in cooperation with the Republic of Chile. The Joint ALMA Observatory is operated by ESO, AUI/NRAO and NAOJ. This program receives funding from the CNRS national program Cosmology and Galaxies. AC, FP, MT, CG acknowledge the support from grant PRIN MIUR 2017. G.C.J. and R.M. acknowledge ERC Advanced Grant 695671 “QUENCH” and support by the Science and Technology Facilities Council (STFC). E.I. acknowledges partial support from FONDECYT through grant N° 1171710. The Cosmic Dawn Center (DAWN) is funded by the Danish National Research Foundation under grant No. 140. S.T. acknowledges support from the ERC Consolidator Grant funding scheme (project Context, grant No. 648179). LV acknowledges funding from the European Union’s Horizon 2020 research and innovation program under the Marie Skłodowska-Curie Grant agreement No. 746119. D.R. acknowledges support from the National Science Foundation under grant numbers AST-1614213 and AST-1910107 and from the Alexander von Humboldt Foundation through a Humboldt Research Fellowship for Experienced Researchers. JDS was supported by the JSPS KAKENHI Grant Number JP18H04346, and the World Premier International Research Center Initiative (WPI Initiative), MEXT, Japan.

References

- Barnabè, M., Dutton, A. A., Marshall, P. J., et al. 2012, *MNRAS*, 423, 1073
- Béthermin, M., Wu, H.-Y., Lagache, G., et al. 2017, *A&A*, 607, A89
- Bouché, N., Murphy, M. T., Kacprzak, G. G., et al. 2013, *Science*, 341, 50
- Bournaud, F., Chapon, D., Teyssier, R., et al. 2011, *ApJ*, 730, 4
- Bouwens, R. J., Illingworth, G. D., Oesch, P. A., et al. 2015, *ApJ*, 803, 34
- Bradač, M., Garcia-Appadoo, D., Huang, K.-H., et al. 2017, *ApJ*, 836, L2
- Capak, P. L., Carilli, C., Jones, G., et al. 2015, *Nature*, 522, 455
- Carilli, C. L. & Walter, F. 2013, *ARA&A*, 51, 105
- Carniani, S., Maiolino, R., Pallottini, A., et al. 2017, *A&A*, 605, A42
- Civano, F., Marchesi, S., Comastri, A., et al. 2016, *ApJ*, 819, 62
- Conselice, C. J. 2014, *ARA&A*, 52, 291
- Croton, D. J., Springel, V., White, S. D. M., et al. 2006, *MNRAS*, 365, 11
- Danielson, A. L. R., Swinbank, A. M., Smail, I., et al. 2017, *The Astrophysical Journal*, 840, 78
- Davé, R., Anglés-Alcázar, D., Narayanan, D., et al. 2019, *MNRAS*, 486, 2827
- Davé, R., Oppenheimer, B. D., & Finlator, K. 2011, *MNRAS*, 415, 11
- Dayal, P., Dunlop, J. S., Maio, U., & Ciardi, B. 2013, *MNRAS*, 434, 1486
- Dayal, P. & Ferrara, A. 2018, *Phys. Rep.*, 780, 1
- De Looze, I., Cormier, D., Leboutteiller, V., et al. 2014, *A&A*, 568, A62
- Dekel, A., Birnboim, Y., Engel, G., et al. 2009, *Nature*, 457, 451
- Dessauges-Zavadsky, M., Zamojski, M., Rujopakarn, W., et al. 2017, *A&A*, 605, A81
- Díaz-Santos, T., Assef, R. J., Blain, A. W., et al. 2018, *Science*, 362, 1034
- Durkalec, A., Le Fèvre, O., de la Torre, S., et al. 2015, *A&A*, 576, L7
- Elvis, M., Civano, F., Vignali, C., et al. 2009, *ApJS*, 184, 158
- Epinat, B., Tasca, L., Amram, P., et al. 2012, *Astronomy and Astrophysics*, 539, A92
- Faisst, A. L., Capak, P. L., Yan, L., et al. 2017, *ApJ*, 847, 21
- Ferrara, A., Vallini, L., Pallottini, A., et al. 2019, *MNRAS*, 489, 1
- Förster Schreiber, N. M., Genzel, R., Bouché, N., et al. 2009, *ApJ*, 706, 1364
- Fujimoto, S., Ouchi, M., Ferrara, A., et al. 2019, arXiv e-prints
- Gabor, J. M., Davé, R., Finlator, K., & Oppenheimer, B. D. 2010, *MNRAS*, 407, 749
- Gabor, J. M., Davé, R., Oppenheimer, B. D., & Finlator, K. 2011, *MNRAS*, 417, 2676
- Genzel, R., Tacconi, L. J., Lutz, D., et al. 2015, *ApJ*, 800, 20
- Giacconi, R., Zirm, A., Wang, J., et al. 2002, *ApJS*, 139, 369
- Ginolfi, M., Jones, G. C., Béthermin, M., et al. 2019, arXiv e-prints, arXiv:1910.04770
- Grogan, N. A., Kocevski, D. D., Faber, S. M., et al. 2011, *ApJS*, 197, 35
- Guo, Y., Ferguson, H. C., Giavalisco, M., et al. 2013, *ApJS*, 207, 24
- Harikane, Y., Ouchi, M., Shibuya, T., et al. 2018, *ApJ*, 859, 84
- Hasinger, G., Capak, P., Salvato, M., et al. 2018, *ApJ*, 858, 77
- Hasinger, G., Cappelluti, N., Brunner, H., et al. 2007, *ApJS*, 172, 29
- Herrera-Camus, R., Bolatto, A., Wolfire, M., et al. 2017, *ApJ*, 835, 201
- Hodge, J. A., Smail, I., Walter, F., et al. 2019, *The Astrophysical Journal*, 876, 130
- Hopkins, P. F., Hernquist, L., Cox, T. J., et al. 2006, *ApJS*, 163, 1
- Hopkins, P. F., Hernquist, L., Cox, T. J., & Kereš, D. 2008, *ApJS*, 175, 356
- Hopkins, P. F., Kereš, D., Oñorbe, J., et al. 2014, *MNRAS*, 445, 581
- Hughes, T. M., Ibar, E., Villanueva, V., et al. 2017, *A&A*, 602, A49
- Ilbert, O., McCracken, H. J., Le Fèvre, O., et al. 2013, *A&A*, 556, A55
- Jones, G. C., Béthermin, M., Fudamoto, Y., et al. 2019, arXiv e-prints, arXiv:1908.07777
- Khusanova, Y., Le Fèvre, O., Cassata, P., et al. 2019, arXiv e-prints
- Koekemoer, A. M., Aussel, H., Calzetti, D., et al. 2007, *ApJS*, 172, 196
- Koekemoer, A. M., Faber, S. M., Ferguson, H. C., et al. 2011, *ApJS*, 197, 36
- Kohandel, M., Pallottini, A., Ferrara, A., et al. 2019, *MNRAS*, 487, 3007
- Laigle, C., McCracken, H. J., Ilbert, O., et al. 2016, *ApJS*, 224, 24
- Le Fèvre, O., Lemaux, B. C., Nakajima, K., et al. 2019, *A&A*, 625, A51
- Le Fèvre, O., Tasca, L. A. M., Cassata, P., et al. 2015, *A&A*, 576, A79
- López-Sanjuan, C., Le Fèvre, O., Tasca, L. A. M., et al. 2013, *A&A*, 553, A78
- Lotz, J. M., Jonsson, P., Cox, T. J., et al. 2011, *ApJ*, 742, 103
- Madau, P. & Dickinson, M. 2014, *ARA&A*, 52, 415
- Maiolino, R., Carniani, S., Fontana, A., et al. 2015, *MNRAS*, 452, 54
- Maiolino, R., Caselli, P., Nagao, T., et al. 2009, *A&A*, 500, L1
- Mantha, K. B., McIntosh, D. H., Brennan, R., et al. 2018, *MNRAS*, 475, 1549
- McAlpine, S., Helly, J. C., Schaller, M., et al. 2016, *Astronomy and Computing*, 15, 72
- McCracken, H. J., Milvang-Jensen, B., Dunlop, J., et al. 2012, *A&A*, 544, A156
- McMullin, J. P., Waters, B., Schiebel, D., Young, W., & Golap, K. 2007, in *Astronomical Society of the Pacific Conference Series*, Vol. 376, *Astronomical Data Analysis Software and Systems XVI*, ed. R. A. Shaw, F. Hill, & D. J. Bell, 127
- Molina, J., Ibar, E., Swinbank, A. M., et al. 2017, *MNRAS*, 466, 892
- Naab, T. & Ostriker, J. P. 2017, *ARA&A*, 55, 59
- Olsen, K., Greve, T. R., Narayanan, D., et al. 2017, *ApJ*, 846, 105
- Pavesi, R., Riechers, D. A., Capak, P. L., et al. 2016, *ApJ*, 832, 151
- Pavesi, R., Riechers, D. A., Faisst, A. L., Stacey, G. J., & Capak, P. L. 2019, *ApJ*, 882, 168
- Pearson, W. J., Wang, L., Hurley, P. D., et al. 2018, *A&A*, 615, A146
- Pineda, J. L., Langer, W. D., Velusamy, T., & Goldsmith, P. F. 2013, *A&A*, 554, A103
- Reddy, N., Dickinson, M., Elbaz, D., et al. 2012, *ApJ*, 744, 154
- Ribeiro, B., Le Fèvre, O., Tasca, L. A. M., et al. 2016, *A&A*, 593, A22
- Riechers, D. A., Carilli, C. L., Capak, P. L., et al. 2014, *ApJ*, 796, 84
- Rodighiero, G., Daddi, E., Baronchelli, I., et al. 2011, *ApJ*, 739, L40
- Sanders, D. B., Salvato, M., Aussel, H., et al. 2007, *ApJS*, 172, 86
- Scoville, N., Abraham, R. G., Aussel, H., et al. 2007a, *ApJS*, 172, 38
- Scoville, N., Aussel, H., Brusa, M., et al. 2007b, *ApJS*, 172, 1
- Scoville, N., Sheth, K., Aussel, H., et al. 2016, *ApJ*, 820, 83
- Silk, J. 1997, *ApJ*, 481, 703
- Silk, J. 2013, *ApJ*, 772, 112
- Silk, J. & Mamon, G. A. 2012, *Research in Astronomy and Astrophysics*, 12, 917
- Smolčić, V., Novak, M., Bondi, M., et al. 2017, *A&A*, 602, A1
- Sobral, D., Matthee, J., Brammer, G., et al. 2019, *MNRAS*, 482, 2422
- Speagle, J. S., Steinhart, C. L., Capak, P. L., & Silverman, J. D. 2014, *ApJS*, 214, 15
- Tacchella, S., Carollo, C. M., Renzini, A., et al. 2015, *Science*, 348, 314
- Tacconi, L. J., Genzel, R., Saintonge, A., et al. 2018, *ApJ*, 853, 179
- Tacconi, L. J., Neri, R., Genzel, R., et al. 2013, *ApJ*, 768, 74
- Tadaki, K., Iono, D., Yun, M. S., et al. 2018, *Nature*, 560, 613
- Taniguchi, Y., Scoville, N., Murayama, T., et al. 2007, *ApJS*, 172, 9
- Tasca, L. A. M., Le Fèvre, O., Hathi, N. P., et al. 2015, *A&A*, 581, A54
- Tasca, L. A. M., Le Fèvre, O., López-Sanjuan, C., et al. 2014, *A&A*, 565, A10
- Tomeczak, A. R., Quadri, R. F., Tran, K.-V. H., et al. 2016, *ApJ*, 817, 118
- Vallini, L., Gallerani, S., Ferrara, A., Pallottini, A., & Yue, B. 2015, *ApJ*, 813, 36
- Ventou, E., Contini, T., Bouché, N., et al. 2017, *A&A*, 608, A9
- Wagg, J., Wiklind, T., Carilli, C. L., et al. 2012, *ApJ*, 752, L30
- Wellons, S., Torrey, P., Ma, C.-P., et al. 2016, *MNRAS*, 456, 1030
- Yue, B., Ferrara, A., Pallottini, A., Gallerani, S., & Vallini, L. 2015, *MNRAS*, 450, 3829
- Zanella, A., Daddi, E., Magdis, G., et al. 2018, *MNRAS*, 481, 1976
- Zhang, Z.-Y., Romano, D., Ivison, R. J., Papadopoulos, P. P., & Matteucci, F. 2018, *Nature*, 558, 260

- ¹ Aix Marseille Université, CNRS, CNES, LAM (Laboratoire d'Astrophysique de Marseille), 13013, Marseille, France
- ² IPAC, California Institute of Technology, 1200 East California Boulevard, Pasadena, CA 91125, USA
- ³ Department of Physics, University of California, Davis, One Shields Ave., Davis, CA 95616, USA
- ⁴ Dipartimento di Fisica e Astronomia, Università di Padova, Vicolo dell'Osservatorio, 3 35122 Padova, Italy
- ⁵ INAF, Osservatorio Astronomico di Padova, vicolo dell'Osservatorio 5, I-35122 Padova, Italy
- ⁶ Kavli Institute for the Physics and Mathematics of the Universe, The University of Tokyo, Kashiwa, Japan 277-8583 (Kavli IPMU, WPI)
- ⁷ Department of Astronomy, University of Geneva, ch. des Maillettes 51, CH-1290 Versoix, Switzerland
- ⁸ Institut de Recherche en Astrophysique et Planétologie - IRAP, CNRS, Université de Toulouse, UPS-OMP, 14, avenue E. Belin, F31400 Toulouse, France
- ⁹ University of Bologna, Department of Physics and Astronomy (DIFA), Via Gobetti 93/2, I-40129, Bologna, Italy
- ¹⁰ INAF - Osservatorio Astrofisico di Arcetri, Largo E. Fermi 5, I-50125, Firenze, Italy
- ¹¹ INAF - Osservatorio di Astrofisica e Scienza dello Spazio di Bologna, via Gobetti 93/3, I-40129, Bologna, Italy
- ¹² Instituto de Investigacion Multidisciplinar en Ciencia y Tecnologia, Universidad de La Serena, Raul Bitran 1305, La Serena, Chile
- ¹³ Departamento de Astronomia, Universidad de La Serena, Av. Juan Cisternas 1200 Norte, La Serena, Chile
- ¹⁴ Centro de Astronomia (CITEVA), Universidad de Antofagasta, Avenida Angamos 601, Antofagasta, Chile
- ¹⁵ Cavendish Laboratory, University of Cambridge, 19 J. J. Thomson Ave., Cambridge CB3 0HE, UK
- ¹⁶ Kavli Institute for Cosmology, University of Cambridge, Madingley Road, Cambridge CB3 0HA, UK
- ¹⁷ Space Telescope Science Institute, 3700 San Martin Drive, Baltimore, MD 21218, USA
- ¹⁸ European Southern Observatory, Av. Alonso de Córdova 3107, Vitacura, Santiago, Chile
- ¹⁹ Astronomy Department, University of Massachusetts, Amherst, MA 01003, USA
- ²⁰ Instituto de Física y Astronomía, Universidad de Valparaíso, Avda. Gran Bretaña 1111, Valparaíso, Chile
- ²¹ Leiden Observatory, Leiden University, PO Box 9500, 2300 RA Leiden, The Netherlands
- ²² Max-Planck Institut für Astronomie, Königstuhl 17, D-69117, Heidelberg, Germany
- ²³ Department of Astronomy, California Institute of Technology, 1200 E. California Blvd., MC 249-17, Pasadena, CA 91125, USA
- ²⁴ Waseda University, Department of Physics, Waseda Research Institute for Science and Engineering Tokyo, Japan
- ²⁵ Research Institute for Science and Engineering, Waseda University, 3-4-1 Okubo, Shinjuku, Tokyo 169-8555, Japan
- ²⁶ National Astronomical Observatory of Japan, 2-21-1, Osawa, Mitaka, Tokyo, Japan
- ²⁷ Cosmic Dawn Center (DAWN), Copenhagen, Denmark
- ²⁸ Niels Bohr Institute, University of Copenhagen, Lyngbyvej 2, DK-2100 Copenhagen, Denmark
- ²⁹ Department of Astronomy, Cornell University, Space Sciences Building, Ithaca, NY 14853, USA
- ³⁰ Department of Astronomy, University of Florida, 211 Bryant Space Sciences Center, Gainesville, FL 32611 USA
- ³¹ University of Florida Informatics Institute, 432 Newell Drive, CISE Bldg E251, Gainesville, FL 32611
- ³² Department of Astronomy, School of Science, The University of Tokyo, 7-3-1 Hongo, Bunkyo, Tokyo 113-0033, Japan
- ³³ Cahill Center for Astrophysics, California Institute of Technology, 1216 East California Boulevard, Pasadena, CA 91125, USA
e-mail: olivier.lefevre@lam.fr

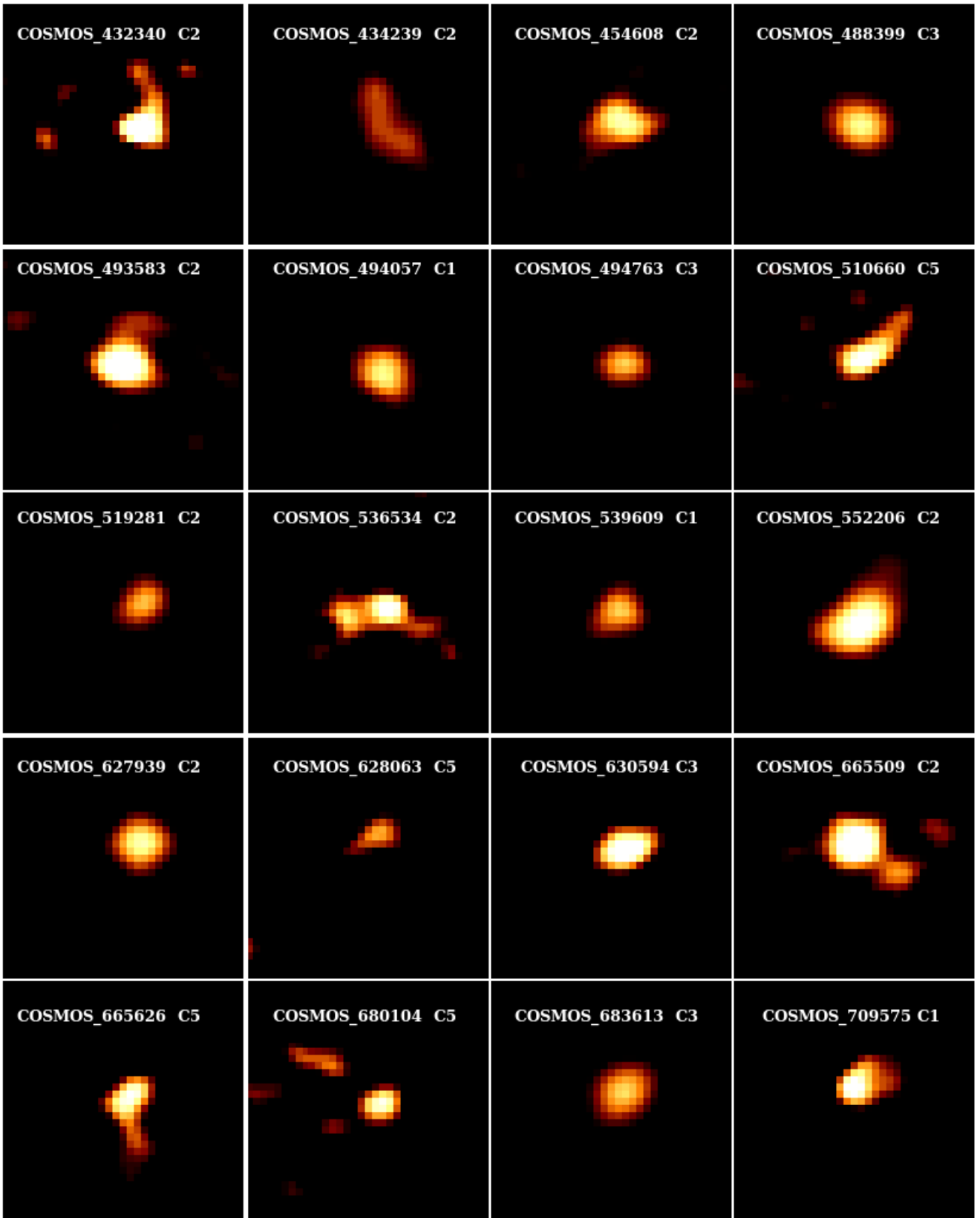


Fig. 6. Velocity-integrated [C II] flux maps obtained collapsing the cube channels containing the [C II] line (see text). Each panel is $5'' \times 5''$ or about 33×33 kpc at the mean redshift $z = 4.7$ of the survey, and centered on the position of the source in the UV rest-frame based on HST-814W images. The object name and morpho-kinematic Class (see Sect. 6) are indicated on top of each sub-panel.

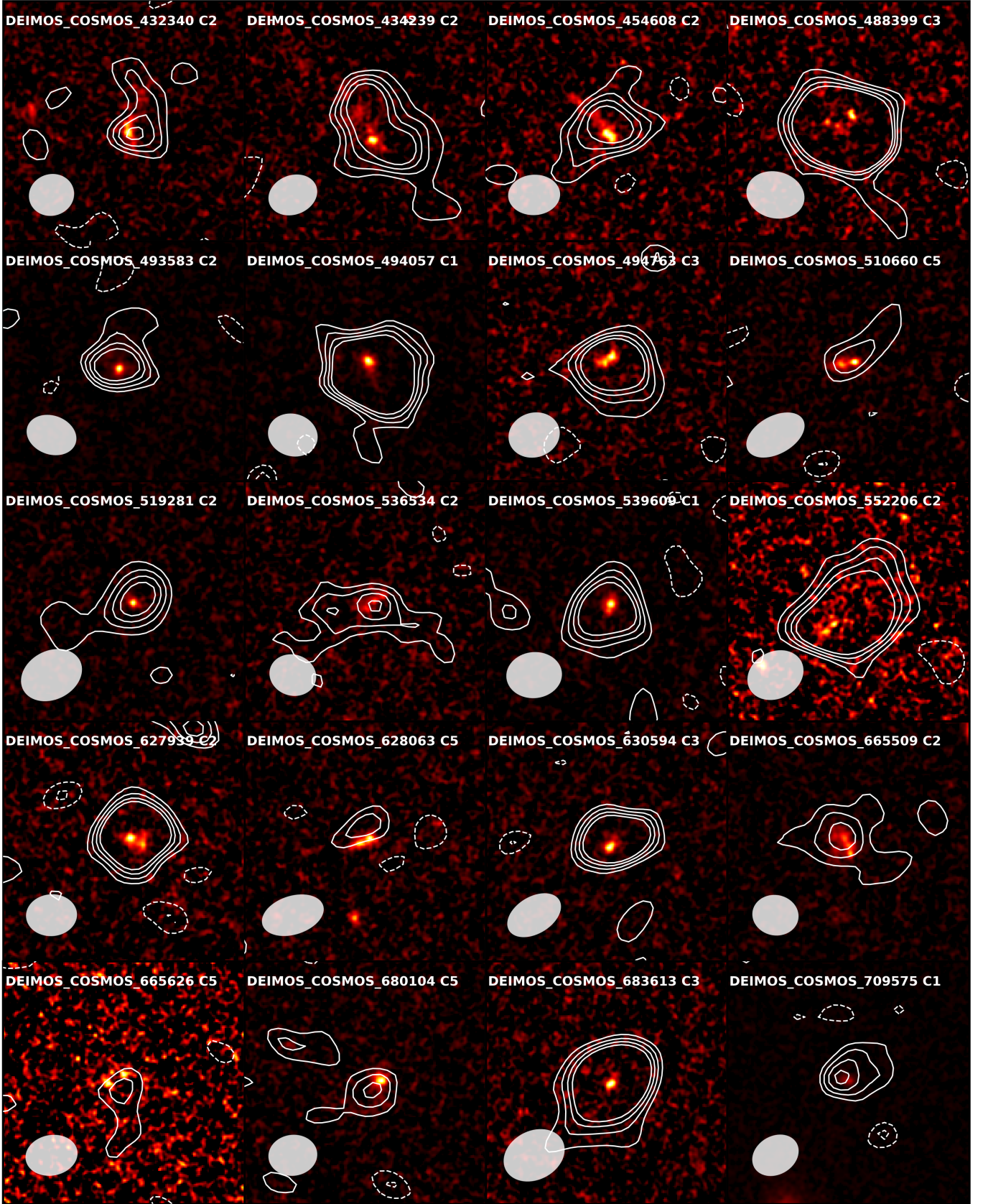


Fig. 7. HST F814W images (Koekemoer et al. 2007, 2011) corresponding to [CII] flux maps in Fig. 6. Each panel is $5'' \times 5''$ or about 33×33 kpc at the mean redshift $z = 4.7$ of the survey, centered on the position of the source in the UV rest-frame HST-814W images. The white contours represent the distribution of the [CII] flux from Fig. 6, and the grey-filled ellipse is the ALMA beam size.

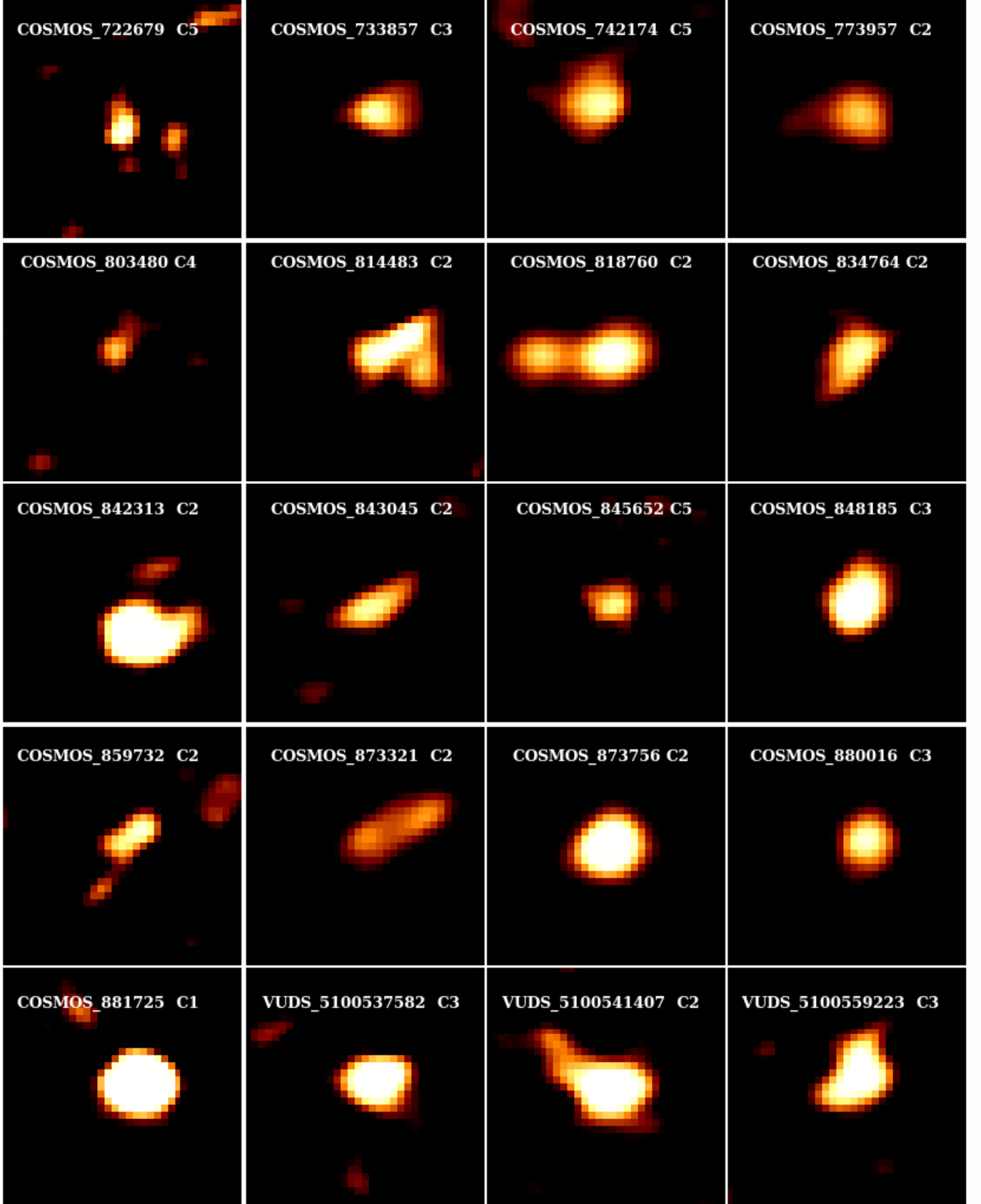


Fig. 8. Velocity-integrated [C II] flux maps obtained collapsing the cube channels containing the [C II] line (see text). Each panel is $5'' \times 5''$ or about 33×33 kpc at the mean redshift $z = 4.7$ of the survey, and centered on the position of the source in the UV rest-frame based on HST-814W images. The object name and morpho-kinematic Class (see Sect. 6) are indicated on top of each sub-panel.

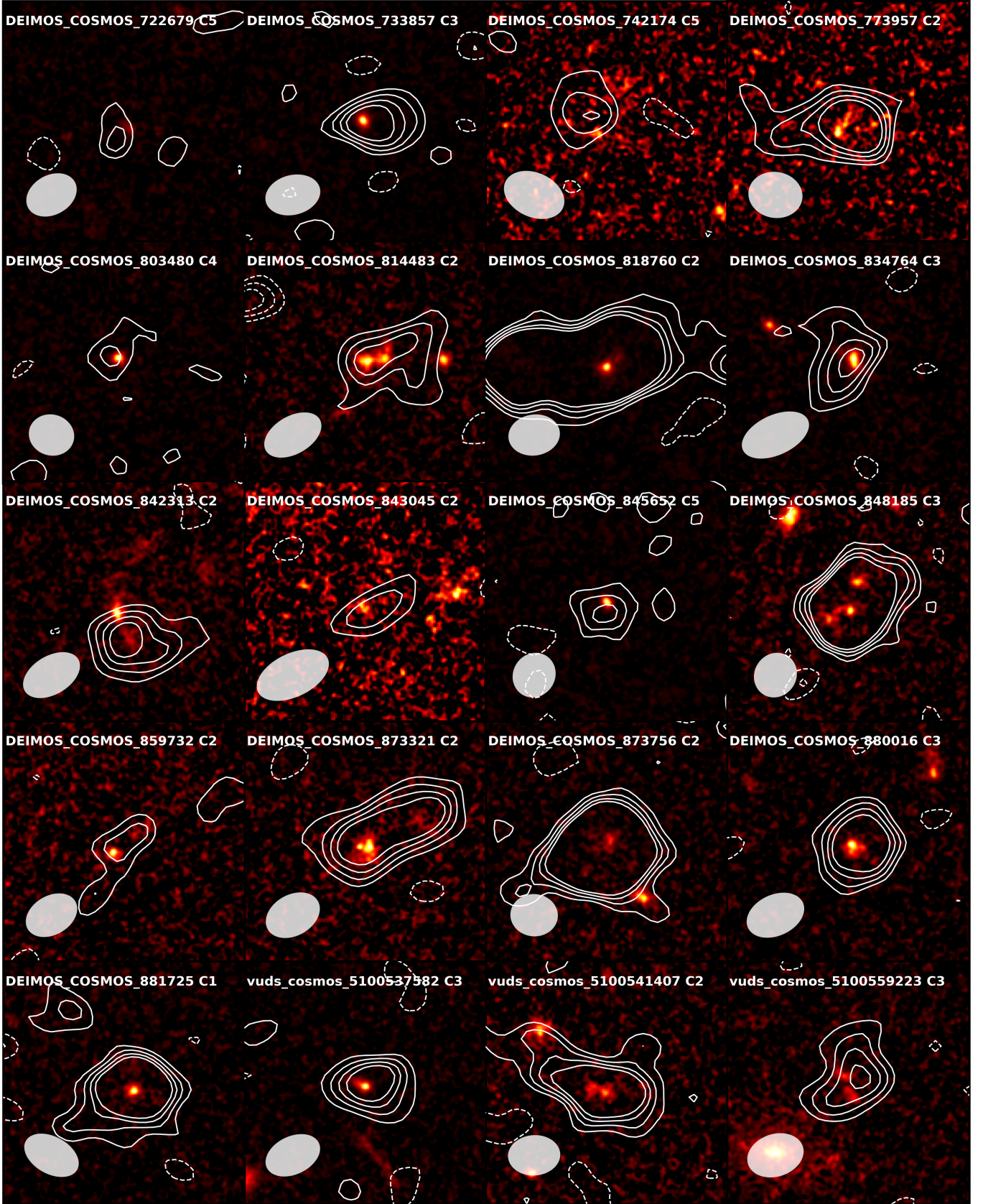


Fig. 9. HST F814W images (Koekemoer et al. 2007, 2011) corresponding to [CII] flux maps in Fig. 8. Each panel is $5'' \times 5''$ or about 33×33 kpc at the mean redshift $z = 4.7$ of the survey, centered on the position of the source in the UV rest-frame HST-814W images. The white contours represent the distribution of the [CII] flux from Fig. 8, and the grey-filled ellipse is the ALMA beam size.

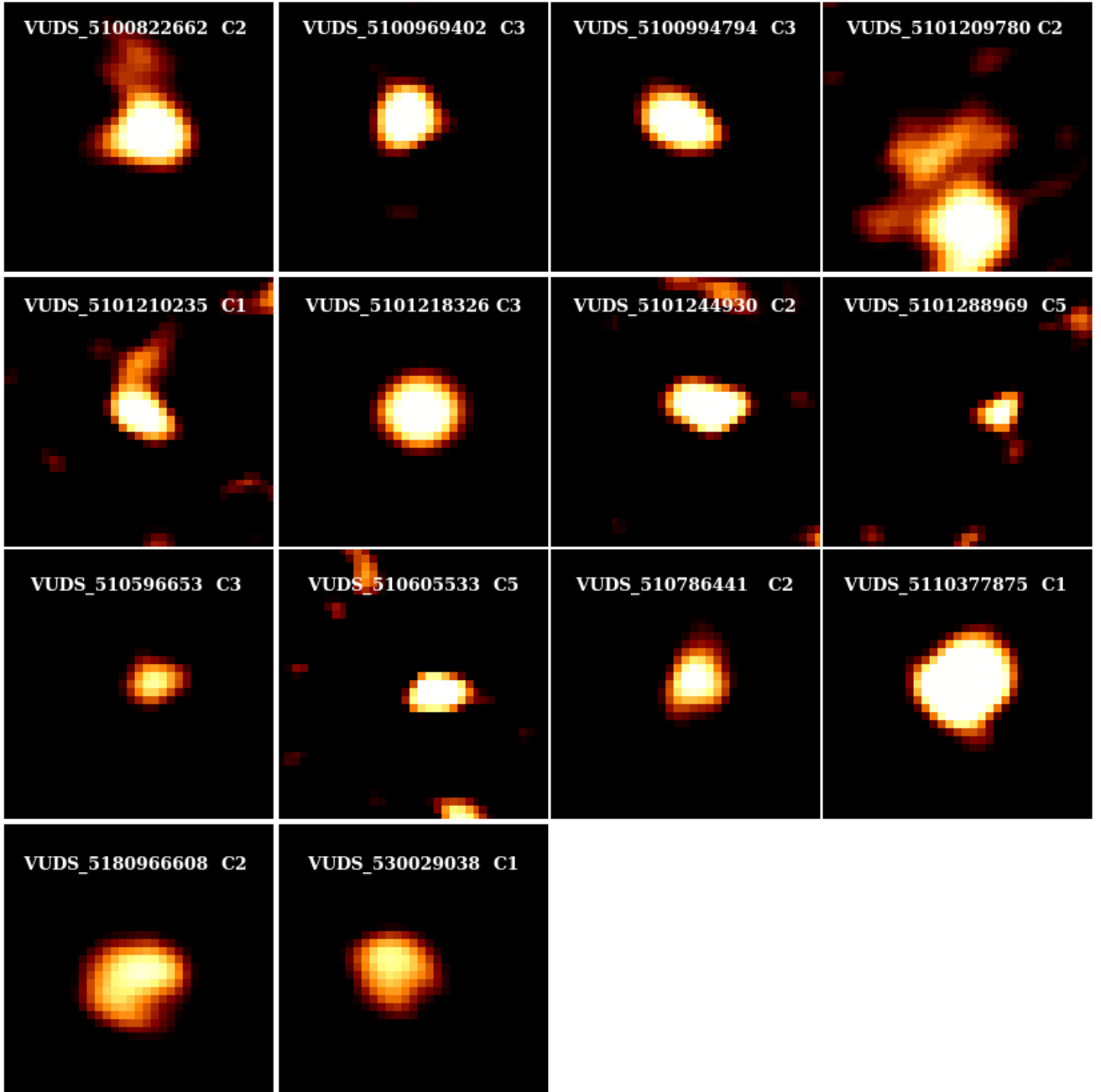


Fig. 10. Velocity-integrated [C II] flux maps obtained collapsing the cube channels containing the [C II] line (see text). Each panel is $5'' \times 5''$ or about 33×33 kpc at the mean redshift $z = 4.7$ of the survey, and centered on the position of the source in the UV rest-frame based on HST-814W images. The object name and morpho-kinematic Class (see Sect. 6) are indicated on top of each sub-panel.

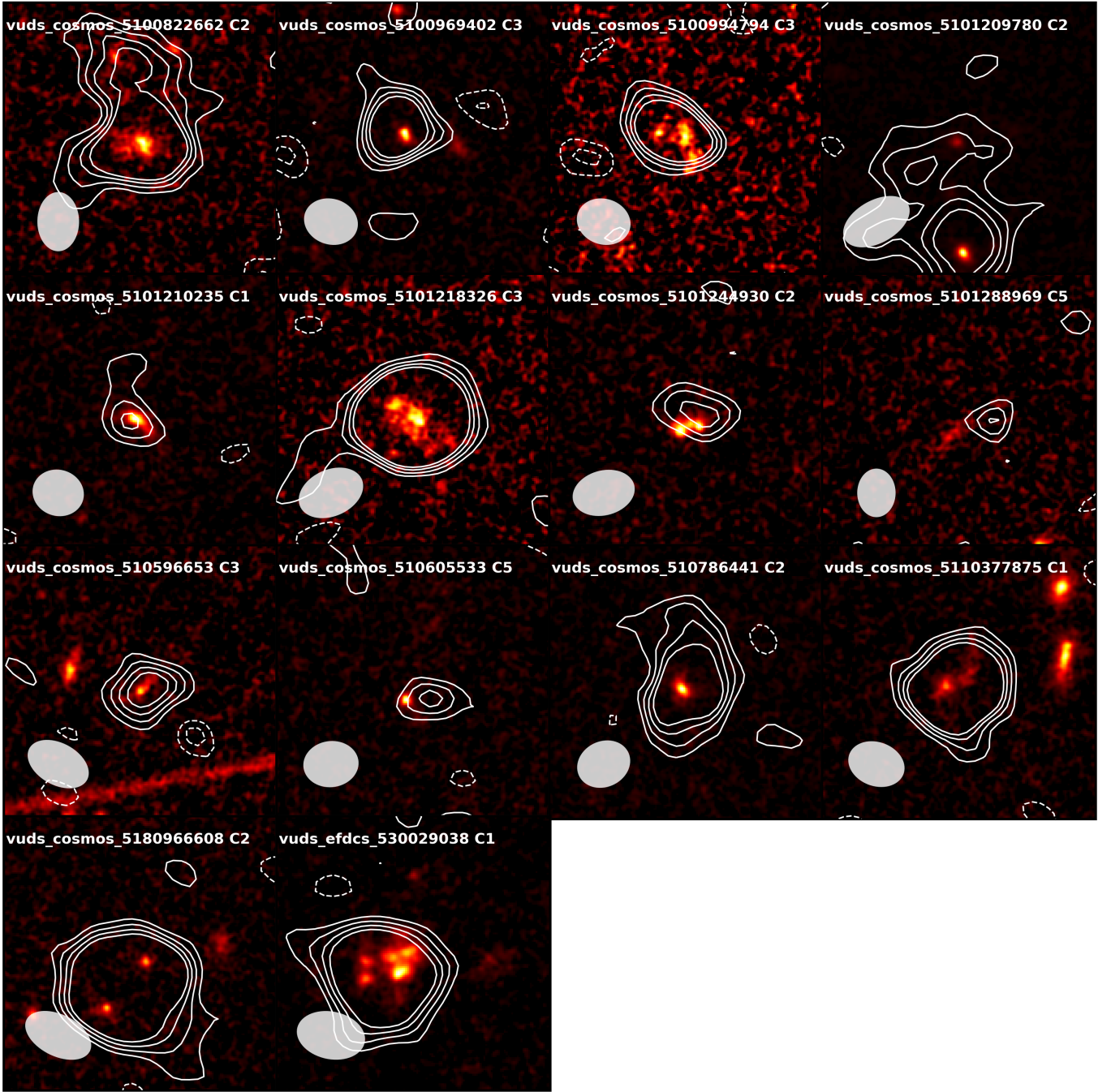


Fig. 11. HST F814W images (Koekemoer et al. 2007, 2011) corresponding to [CII] flux maps in Fig. 10. Each panel is $5'' \times 5''$ or about 33×33 kpc at the mean redshift $z = 4.7$ of the survey, centered on the position of the source in the UV rest-frame HST-814W images. The white contours represent the distribution of the [CII] flux from Fig. 10, and the grey-filled ellipse is the ALMA beam size.

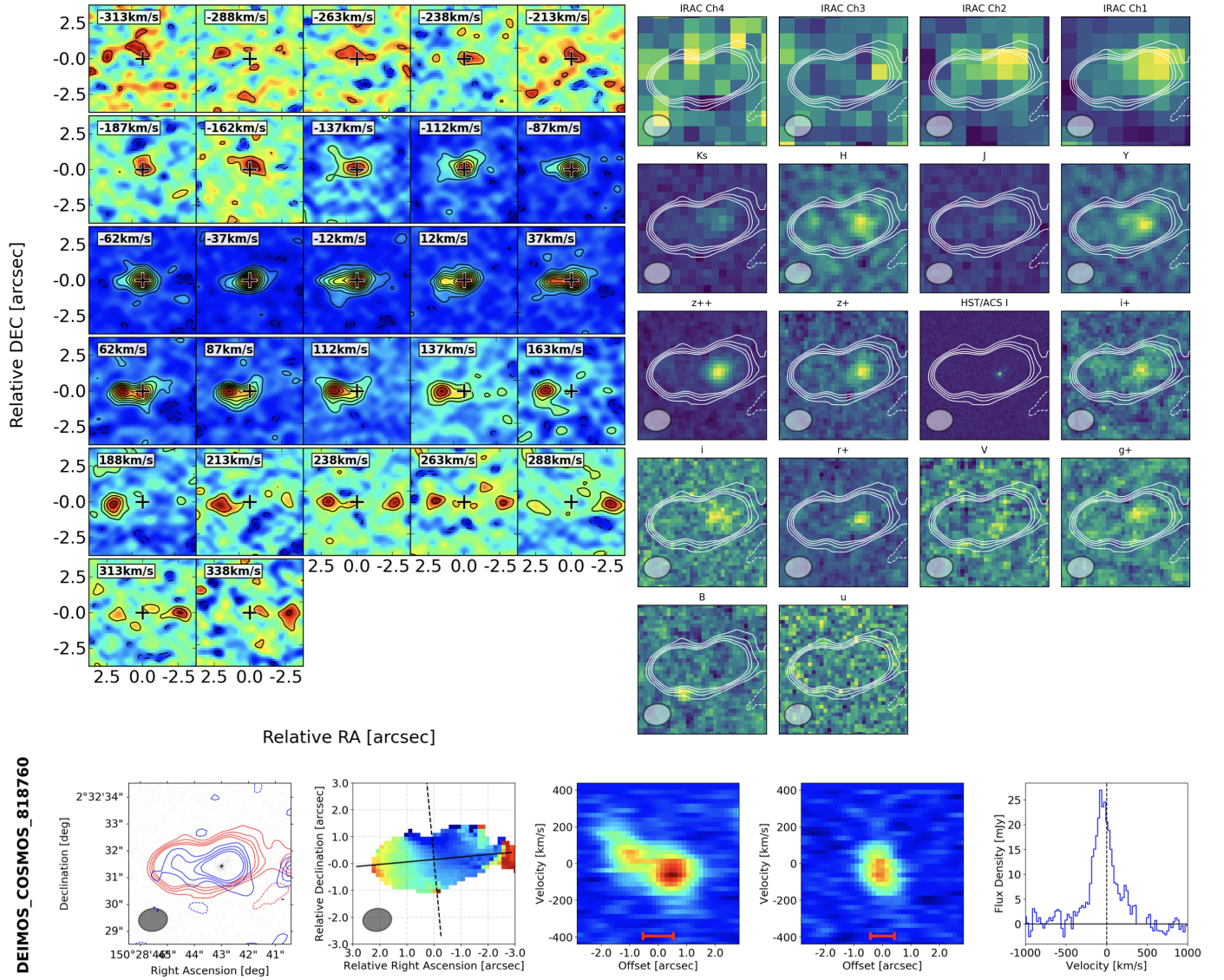


Fig. 12. Summary panel with all information available to classify galaxies. *Top left:* Velocity channel maps, in 25km/s velocity intervals. *Top right:* Optical and NIR images, with contours from the [CII] emission. *Bottom, left to right:* flux map in [CII] (red contours) and continuum emission (blue contours) overlaid on top of the i-band F814W HST image; velocity map with major and minor axes used to produce the PV diagram of the next two panels on the right; [CII] line emission in velocity ($V=0$ being from the UV-derived spectroscopic redshift). This galaxy has been classified as a merger (Class 2).

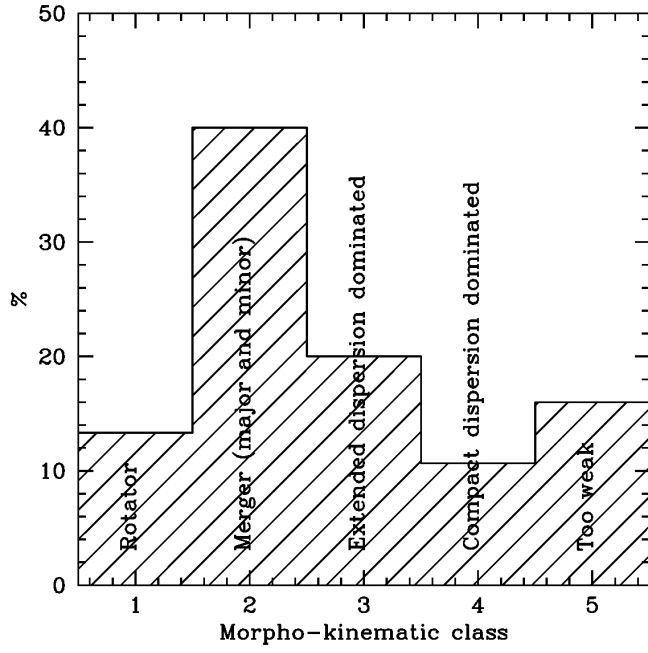


Fig. 13. The distribution of morpho-kinematic classes in the ALPINE sample for sources with [CII] measured at more than 3.5σ above the noise.

Table 1. Properties of the ALPINE sample of galaxies with [CII] detected above 3.5σ , including position, spectroscopic redshift z_{spec} derived from the UV spectra, signal-to-noise ratio SNR, as well as the object class as described in Sect. 6

ALPINE ID	α_{2000}	δ_{2000}	z_{spec}	SNR([CII])	morpho-kinematic class
CANDELS-GOODSS-12	53.2250	-27.8336	4.4750	4.42	5
CANDELS-GOODSS-14	53.0789	-27.8841	5.7230	4.57	4
CANDELS-GOODSS-21	53.0498	-27.6993	4.4820	4.23	4
CANDELS-GOODSS-32	53.0708	-27.6872	5.6820	12.25	2
CANDELS-GOODSS-38	53.0663	-27.6901	4.5270	4.74	2
CANDELS-GOODSS-42	53.1659	-27.8828	5.543	3.69	5
CANDELS-GOODSS-47	53.1885	-27.8195	5.7140	4.02	4
CANDELS-GOODSS-75	53.1357	-27.7982	5.7070	4.76	4
DEIMOS-COSMOS-274035	149.8853	1.7016	5.7380	4.43	4
DEIMOS-COSMOS-308643	150.3611	1.7573	5.1370	7.71	2
DEIMOS-COSMOS-351640	150.3712	1.8249	5.4300	5.68	3
DEIMOS-COSMOS-357722	149.9668	1.8350	4.5400	3.57	4
DEIMOS-COSMOS-372292	149.9131	1.8578	4.5330	9.60	2
DEIMOS-COSMOS-378903	150.2976	1.8684	4.5680	4.59	2
DEIMOS-COSMOS-396844	150.2485	1.8964	5.6780	12.09	1
DEIMOS-COSMOS-400160	150.2671	1.9014	4.4340	4.45	4
DEIMOS-COSMOS-403030	150.0273	1.9059	5.6340	5.03	2
DEIMOS-COSMOS-416105	150.6902	1.9267	5.6750	5.29	1
DEIMOS-COSMOS-417567	150.5172	1.9290	5.7260	6.39	2
DEIMOS-COSMOS-422677	150.4977	1.9369	5.5800	7.14	2
DEIMOS-COSMOS-430951	150.3268	1.9508	4.4430	4.12	5
DEIMOS-COSMOS-432340	150.5397	1.9515	5.6840	5.49	2
DEIMOS-COSMOS-434239	150.3213	1.9554	4.4300	7.35	2
DEIMOS-COSMOS-454608	150.6807	1.9891	4.4070	6.45	2
DEIMOS-COSMOS-471063	150.065	2.0155	5.718	3.52	5
DEIMOS-COSMOS-488399	150.7548	2.0433	4.4920	26.18	3
DEIMOS-COSMOS-493583	150.0974	2.0512	4.5780	8.29	2
DEIMOS-COSMOS-494057	149.6187	2.0518	4.4610	17.11	1
DEIMOS-COSMOS-494763	150.0213	2.0534	5.3900	10.51	3
DEIMOS-COSMOS-510660	149.9715	2.0772	5.6850	4.00	5
DEIMOS-COSMOS-519281	149.7537	2.0910	5.7180	6.73	2
DEIMOS-COSMOS-536534	149.9718	2.1182	5.6450	5.01	2
DEIMOS-COSMOS-539609	149.7803	2.1226	5.6780	8.91	1
DEIMOS-COSMOS-552206	149.6116	2.1408	4.5160	14.83	2
DEIMOS-COSMOS-627939	150.2702	2.2539	5.5400	12.99	2
DEIMOS-COSMOS-628063	150.2177	2.2544	5.2380	3.85	5
DEIMOS-COSMOS-630594	150.1358	2.2579	5.6490	11.16	3
DEIMOS-COSMOS-665509	149.7352	2.3109	4.5540	4.83	2
DEIMOS-COSMOS-665626	150.3093	2.3117	4.5010	4.42	5
DEIMOS-COSMOS-680104	150.2923	2.3322	5.5700	4.18	5
DEIMOS-COSMOS-683613	150.0393	2.3372	5.6940	13.63	3
DEIMOS-COSMOS-709575	149.9461	2.3758	5.1700	5.47	1
DEIMOS-COSMOS-722679	149.9371	2.3961	5.5500	4.04	5
DEIMOS-COSMOS-733857	150.3330	2.4132	4.4190	7.33	3
DEIMOS-COSMOS-742174	150.1631	2.4257	5.5140	4.76	5
DEIMOS-COSMOS-773957	150.2919	2.4747	4.5630	8.47	2
DEIMOS-COSMOS-803480	149.9886	2.5203	5.6620	3.75	4
DEIMOS-COSMOS-814483	150.3630	2.5363	5.8660	4.65	2
DEIMOS-COSMOS-818760	150.4786	2.5420	4.5280	26.66	2
DEIMOS-COSMOS-834764	149.8989	2.5668	4.5320	5.44	3
DEIMOS-COSMOS-842313	150.2272	2.5762	4.5390	6.52	2
DEIMOS-COSMOS-843045	150.0515	2.5787	5.6850	4.06	2
DEIMOS-COSMOS-845652	150.2150	2.5826	5.1210	4.86	5
DEIMOS-COSMOS-848185	150.0896	2.5864	4.4470	18.33	3
DEIMOS-COSMOS-859732	150.0020	2.6054	4.5290	4.26	2
DEIMOS-COSMOS-873321	150.0169	2.6266	4.5830	7.55	2
DEIMOS-COSMOS-873756	150.0113	2.6278	5.6800	32.59	2
DEIMOS-COSMOS-880016	149.9798	2.6380	4.5320	8.63	3
DEIMOS-COSMOS-881725	150.0564	2.64	5.5360	12.27	1

Table 1. continued.

ALPINE ID	α_{2000}	δ_{2000}	z_{spec}	SNR([CII])	morpho-kinematic class
VUDS-COSMOS-5100537582	150.3896	1.8380	4.4150	8.12	3
VUDS-COSMOS-5100541407	150.2538	1.8094	5.7580	11.36	2
VUDS-COSMOS-5100559223	150.2214	1.8649	4.5470	5.88	3
VUDS-COSMOS-5100822662	149.7413	2.0809	5.6410	14.89	2
VUDS-COSMOS-5100969402	150.3338	2.2837	4.5170	11.00	3
VUDS-COSMOS-5100994794	150.1716	2.2873	4.5800	12.03	3
VUDS-COSMOS-5101209780	150.3896	2.3694	5.6830	4.29	2
VUDS-COSMOS-5101210235	150.3817	2.3660	4.5110	4.33	1
VUDS-COSMOS-5101218326	150.3021	2.3146	5.6910	26.58	3
VUDS-COSMOS-5101244930	150.1985	2.3006	4.5420	5.04	2
VUDS-COSMOS-5101288969	149.8776	2.3315	4.5840	4.24	5
VUDS-COSMOS-510596653	149.8262	1.9381	4.5540	6.18	3
VUDS-COSMOS-510605533	149.8525	1.8785	4.5040	4.91	5
VUDS-COSMOS-510786441	150.1429	1.9982	4.5260	11.09	2
VUDS-COSMOS-5110377875	150.3847	2.4084	4.5520	18.50	1
VUDS-COSMOS-5180966608	150.4061	2.1398	5.8170	12.46	2
VUDS-ECDFS-530029038	53.0794	-27.8772	5.3100	9.22	1

Table 2. [CII] emission limits for the undetected sample

ALPINE ID	α_{2000}	δ_{2000}	z_{spec}	3σ limit $Jy.km.s^{-1}$
DEIMOS-COSMOS-206253	150.2793	1.5936	4.4750	0.189
DEIMOS-COSMOS-224751	149.9672	1.6231	5.7230	0.094
DEIMOS-COSMOS-298678	150.3621	1.7417	5.6820	0.141
DEIMOS-COSMOS-328419	149.9792	1.7891	5.7160	0.180
DEIMOS-COSMOS-336830	150.4004	1.8018	5.7140	0.109
DEIMOS-COSMOS-406956	150.5367	1.9125	5.6780	0.146
DEIMOS-COSMOS-412589	150.4034	1.9213	4.4340	0.186
DEIMOS-COSMOS-420065	150.3493	1.9334	5.7260	0.101
DEIMOS-COSMOS-421062	150.0356	1.9346	5.5800	0.104
DEIMOS-COSMOS-431067	150.3686	1.9511	4.4300	0.210
DEIMOS-COSMOS-442844	149.9992	1.9704	4.4920	0.179
DEIMOS-COSMOS-460378	150.0474	1.9984	5.3900	0.148
DEIMOS-COSMOS-470116	149.9336	2.0141	5.6850	0.098
DEIMOS-COSMOS-471063	150.065	2.0155	5.718	0.101
DEIMOS-COSMOS-472215	150.0832	2.0176	5.6450	0.154
DEIMOS-COSMOS-503575	149.7219	2.0670	5.6490	0.097
DEIMOS-COSMOS-549131	150.1789	2.1368	5.5500	0.153
DEIMOS-COSMOS-550156	150.2520	2.1383	4.4190	0.191
DEIMOS-COSMOS-567070	150.2748	2.1635	4.5630	0.235
DEIMOS-COSMOS-576372	149.9782	2.1776	5.6620	0.126
DEIMOS-COSMOS-586681	150.0366	2.1935	5.8660	0.220
DEIMOS-COSMOS-592644	150.1109	2.2017	4.5280	0.194
DEIMOS-COSMOS-628137	149.9772	2.2546	5.6850	0.106
DEIMOS-COSMOS-629750	150.1430	2.2568	5.1210	0.148
DEIMOS-COSMOS-743730	150.3021	2.4285	4.5170	0.158
DEIMOS-COSMOS-761315	149.9522	2.4557	4.5800	0.152
DEIMOS-COSMOS-787780	149.9861	2.4967	4.5110	0.210
DEIMOS-COSMOS-790930	150.3657	2.5017	5.6910	0.096
DEIMOS-COSMOS-838532	150.4321	2.5725	4.5260	0.191
DEIMOS-COSMOS-869970	150.1041	2.6217	5.2000	0.105
DEIMOS-COSMOS-910650	150.0938	2.6843	5.6620	0.102
DEIMOS-COSMOS-920848	149.8909	2.6989	4.5540	0.202
DEIMOS-COSMOS-926434	150.1091	2.7065	4.4500	0.200
DEIMOS-COSMOS-933876	149.9012	2.7193	4.4170	0.200
VUDS-COSMOS-5101013812	150.2099	2.1631	4.4200	0.203
VUDS-COSMOS-510148750	149.8428	1.9929	4.5062	0.143
VUDS-COSMOS-510327576	150.1106	1.7850	4.5600	0.223
VUDS-COSMOS-510581738	149.9088	1.8776	4.5000	0.178
VUDS-COSMOS-5131465996	150.2200	2.4655	4.4637	0.174
CANDELS-GOODSS-8	53.1568	-27.8396	5.5180	0.108
CANDELS-GOODSS-19	53.0957	-27.7747	4.5000	0.157
CANDELS-GOODSS-37	53.1734	-27.8183	4.5200	0.151
CANDELS-GOODSS-42	53.16591	-27.8828	5.543	1064
CANDELS-GOODSS-57	53.1626	-27.8731	5.5590	0.116
CANDELS-GOODSS-8	53.1568	-27.8396	5.5180	0.108